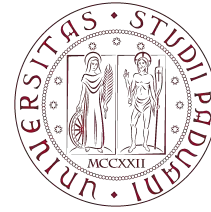
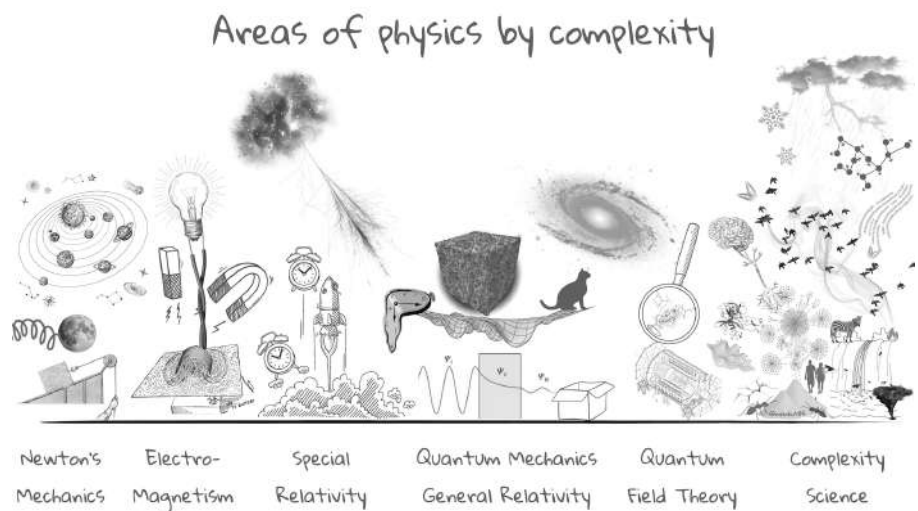


Final Report

Physics of Complex Networks: Structure and Dynamics



UNIVERSITÀ
DEGLI STUDI
DI PADOVA



Project #6: Dynamics on networks

Bergamin Eleonora, Campagnola Stefano

Chiloiro Marco, Pedrazzi Matteo

SunPraisers

Last update: September 6, 2023

Contents

1	Turing Patterns	1
1.1	Introduction	1
1.2	Theoretical background	1
1.3	Turing instability and critical Turing modes	2
1.4	Patterns formation	2
1.5	Mean-field approximation	3
1.6	Appendix	3
1.6.1	Diffusive flux	3
1.6.2	Mimura-Murray model	4
1.6.3	Linear stability analysis	4
1.6.4	Critical Turing modes	6
1.6.5	Stationary patterns and mean-field bifurcation plots	7
2	The Kuramoto model	9
2.1	Introduction	9
2.2	Theoretical background	9
2.3	Emergence of spontaneous synchronization	10
2.4	Stability of the synchronous state	11
2.5	Topological scales emergence by synchronization	11
2.6	Appendix	12
2.6.1	Linearized dynamics of the Kuramoto model	14
3	Swarmalators dynamic	16
3.1	Introduction	16
3.2	Theoretical background	16
3.3	Basic model	17
3.4	Forced model	17
3.5	Time varying interaction model	18
3.6	Vicsek model	18
3.7	Appendix	19
3.7.1	Lattice model	20
3.7.2	Vicsek model	21
4	Bibliography	23

1 | Turing Patterns

Task leader(s): *Pedrazzi Matteo*

1.1 | Introduction

Turing patterns, named after the eminent mathematician and biologist Alan Turing, represent one of the most interesting phenomena in the field of pattern formation and nonlinear dynamics. These intricate, self-organizing structures emerge in various natural systems, ranging from chemical reactions and animal coat markings to ecological landscapes and embryonic development.

Turing patterns are characterized by their ability to self-assemble complex spatial structures from initially homogeneous states. This remarkable property arises from the nonlinear interactions between two or more diffusing substances, often referred to as activators and inhibitors, which engage in a delicate dance of mutual activation and inhibition.

Turing Patterns have also been studied on top of networks, initially considering only regular lattices and generally small networks. Here from [4] we reproduce results for Turing Patterns on large random networks, with new perspective on self-organization phenomena in systems organized as complex networks. This paper will focus on the conditions needed to develop these behaviours and on the simulation of the results, considering different parameters settings and network characteristics.

1.2 | Theoretical background

In our study, we consider the analogue on networks for the equations of activator-inhibitor system in classical media, where activator and inhibitor species occupy discrete nodes of a network and are transported by diffusion over links connecting them. By introducing the network Laplacian matrix $L_{ij} = A_{ij} - k_i \delta_{ij}$, where A is the adjacency matrix and k_i the degree of node i , the diffusive flux of species u to node i is expressed as $\sum_{j=1}^N L_{ij} u_j$, and similarly for v (see Appendix section, 1.6.1). The equations describing network-organized activator-inhibitor systems are:

$$\frac{\partial}{\partial t} u_i(t) = f(u_i, v_i) + \epsilon \sum_{j=1}^N L_{ij} u_j \quad (1.1)$$

$$\frac{\partial}{\partial t} v_i(t) = g(u_i, v_i) + \sigma \epsilon \sum_{j=1}^N L_{ij} v_j \quad (1.2)$$

where ϵ and $\sigma \epsilon$ are the diffusion constants of the activator and the inhibitor species respectively, while functions $f(u_i, v_i)$ and $g(u_i, v_i)$ specify their local dynamics on the

i -th node. In particular the Mimura-Murray model for prey-predator populations has been chosen in this work, with its details showed in Appendix 1.6.2.

1.3 | Turing instability and critical Turing modes

The uniform stationary state (\bar{u}, \bar{v}) can become unstable because of Turing instability, which sets in as the ratio of the two diffusion constants σ exceeds a certain threshold σ_c , leading to spontaneous development of alternating activator-rich and activator-poor domains from the uniform background. From the linear stability analysis performed on the uniform stationary state with respect to non-uniform perturbations, in addition to the value of this threshold, we can determine the linear growth rates λ_α of each mode $\alpha = 1, \dots, N$, linked to the Laplacian eigenvalues Λ_α and eigenvectors $\vec{\phi}^{(\alpha)} = (\phi_1^{(\alpha)}, \dots, \phi_N^{(\alpha)})$, determined by the relation $\sum_{j=1}^N L_{ij} \phi_j^{(\alpha)} = \Lambda_\alpha \phi_i^{(\alpha)}$. The main idea and principal steps of the derivation are shown in Appendix 1.6.3, with also the figure presenting the linear growth rates as a function of the Laplacian eigenvalues for three different values of diffusive mobility ϵ .

The role of Laplacian eigenvectors becomes crucial when a Turing pattern starts to grow slightly after the instability threshold: the activator and inhibitor distribution are then determined by the critical Laplacian eigenvector. In Figure 1.2 we can observe that the localization on the graph is different for the critical Laplacian eigenvectors: for small values of diffusion mobility ϵ the hubs are more likely to differentiate (top), while on the opposite for higher values of ϵ the nodes with lower degrees are the ones undergoing differentiation (bottom). This is due to the localization of Laplacian eigenvectors, which on random networks tend to localize on subsets of nodes with close degrees. Since from the linear stability analysis we have that $\Lambda_{\alpha_c} \propto 1/\epsilon$, and since for scale-free networks Laplacian eigenvectors possess a characteristic localization degree $\bar{k}_\alpha \simeq \Lambda_\alpha$, we get the scaling law $\bar{k}_\alpha \propto 1/\epsilon$, showing that the characteristic localization degree of differentiated nodes is directly correlated to the diffusion mobility, being a decreasing function of it.

1.4 | Patterns formation

After an initial short period in which the differences with respect to the critical mode are small, the nonlinear process leads to the formation of stationary Turing patterns which are shifted away from the critical one. We chose to reproduce the Mimura-Murray model on a random scale-free network of size $N = 1000$ and mean degree $\langle k \rangle \simeq 20$, generated by using the Barabási-Albert linear preferential attachment algorithm. The coefficients used are $\epsilon = 0.12$ and $\sigma = 15.6$, that is slightly above the instability threshold, and also $\sigma = 30$ to see if the developed separation effect for the nodes is stronger. Finally we ran some tests also on a different type of synthetic random network with a different degree distribution, namely the Erdős-Rényi model, keeping fixed the network size $N = 1000$ and the mean degree $\langle k \rangle \simeq 20$.

The figures representing the simulated Turing patterns for activator and inhibitor, using different values of σ , are reported in Appendix 1.6.5, showing also the position on the network of the most and least differentiated nodes. From Figure 1.3 we see that in the asymptotic state, the nodes are divided into two groups and, given that in the

plot the nodes have been ordered by decreasing degree, we can see only a subset of the nodes with lower degrees are undergoing differentiation from the initial state.

Results are presented in 1.5 for the random ER network. Given the homogeneous and narrower degree distribution typical of this graph, we could have expected smoother and flatter patterns, probably limited by the relatively small dimension of the network considered.

1.5 | Mean-field approximation

To have a better understanding of the developed Turing patterns above the instability threshold, one can also apply the mean-field approach, which has the great advantage of not being dependent on the detailed information from the network. The idea behind this approach is that the local field felt by each node $h_i^{(u)} = \sum_{j=1}^N A_{ij}u_j$ can be approximated as $h_i^{(u)} \sim k_i H^{(u)}$, where $H^{(u)}$ is the constant global mean field computed as $H^{(u)} = \sum_{j=1}^N k_j u_j / k_{tot}$, weighting the importance of each node with its degree. The same is holding for v . Finally defining a bifurcation parameter $\beta(i) = \epsilon k_i$ controlling the individual nodes dynamics, one can drop the indices and the following couple of mean-field equations can be used to fit the stationary Turing pattern described above in all the network nodes:

$$\frac{\partial}{\partial t} u(t) = f(u, v) + \beta(H^{(u)} - u) \quad (1.3)$$

$$\frac{\partial}{\partial t} v(t) = g(u, v) + \sigma \beta(H^{(v)} - v) \quad (1.4)$$

The results are presented in Appendix 1.6.5 together with the stationary Turing patterns. Figures show that this approximation is able to fit satisfactorily the nodes differentiation, both for the inhibitor and activator species and also for different diffusion ratios σ .

1.6 | Appendix

1.6.1 Diffusive flux

The diffusive flux of species u to node i considering all the contributes coming from its neighbours is expressed as

$$\begin{aligned} \sum_{j=1}^N A_{ij}(u_j - u_i) &= \sum_{j=1}^N A_{ij}u_j - u_i \sum_{j=1}^N A_{ij} \\ &= \sum_{j=1}^N A_{ij}u_j - k_i u_i \\ &= \sum_{j=1}^N (A_{ij} - k_i \delta_{ij})u_j \\ &= \sum_{j=1}^N L_{ij}u_j \end{aligned} \quad (1.5)$$

The same steps can be followed also for the diffusive flux of inhibitor species v .

1.6.2 Mimura-Murray model

The Mimura-Murray model is a mathematical model used to describe the dynamics of activator-inhibitor systems, developed to study the interaction between densities of prey and predator species, here u and v . The nonlinear functions used in this model from [4] are:

$$f(u, v) = \{(a + b \cdot u - u^2)/c - v\}u \quad (1.6)$$

$$g(u, v) = \{u - (1 + d \cdot v)\}v \quad (1.7)$$

with parameters $a = 35$, $b = 16$, $c = 9$, and $d = 2/5$, having a fixed point $(\bar{u}, \bar{v}) = (5, 10)$, where $f(\bar{u}, \bar{v}) = g(\bar{u}, \bar{v}) = 0$, corresponding to the uniform stationary state of the system.

1.6.3 Linear stability analysis

Introducing small perturbations δu_i and δv_i to the uniform state (\bar{u}, \bar{v}) and substituting into equations 1.1 and 1.2, a set of coupled linearized differential equations is obtained for the perturbations:

$$\frac{\partial}{\partial t} \delta u_i = f_u \delta u_i + f_v \delta v_i + \epsilon \sum_{j=1}^N L_{ij} u_j \quad (1.8)$$

$$\frac{\partial}{\partial t} \delta v_i = g_u \delta u_i + g_v \delta v_i + \sigma \epsilon \sum_{j=1}^N L_{ij} v_j \quad (1.9)$$

where the first terms are indicating the partial derivatives of the function $f(u, v)$ and $g(u, v)$ w.r.t. u and v , computed in the uniform state (\bar{u}, \bar{v}) .

By expanding the perturbations over a set of Laplacian eigenvectors $\vec{\phi}^{(\alpha)}$

$$\delta u_i = \sum_{\alpha=1}^N c_{\alpha} \exp(\lambda_{\alpha} t) \phi_i^{(\alpha)} \quad (1.10)$$

$$\delta v_i = \sum_{\alpha=1}^N c_{\alpha} B_{\alpha} \exp(\lambda_{\alpha} t) \phi_i^{(\alpha)} \quad (1.11)$$

and then substituting back into equations 1.8 and 1.9 we get an eigenvalue equation for each mode α , whose characteristic equation is

$$(f_u + \epsilon \Lambda_{\alpha} - \lambda_{\alpha})(g_v + \sigma \epsilon \Lambda_{\alpha} - \lambda_{\alpha}) - f_v g_u = 0 \quad (1.12)$$

From equation 1.12 we can derive the pair of conjugate growth rates of each Laplacian mode, of which the upper branch is the one always used

$$\lambda_{\alpha} = \frac{1}{2} \left[f_u + g_v + (1 + \sigma) \epsilon \Lambda_{\alpha} \pm \sqrt{4 f_v g_u + (f_u - g_v + (1 - \sigma) \epsilon \Lambda_{\alpha})^2} \right] \quad (1.13)$$

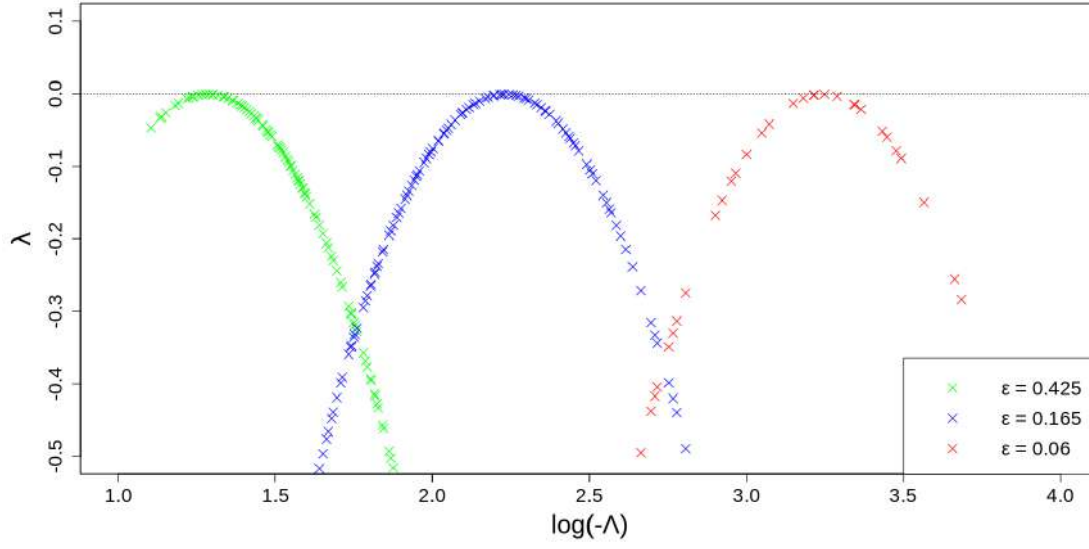


Figure 1.1: Linear growth rates λ_α as a function of the Laplacian eigenvalues Λ_α . Three critical modes are showed, corresponding to three different values of diffusional mobility ϵ . The curves first touch the horizontal axis at $\Lambda = \Lambda_c$ and the Laplacian mode $\phi^{(\alpha_c)}$ possessing the Laplacian eigenvalue Λ_{α_c} that is closest to Λ_c , becomes critical.

1.6.4 Critical Turing modes

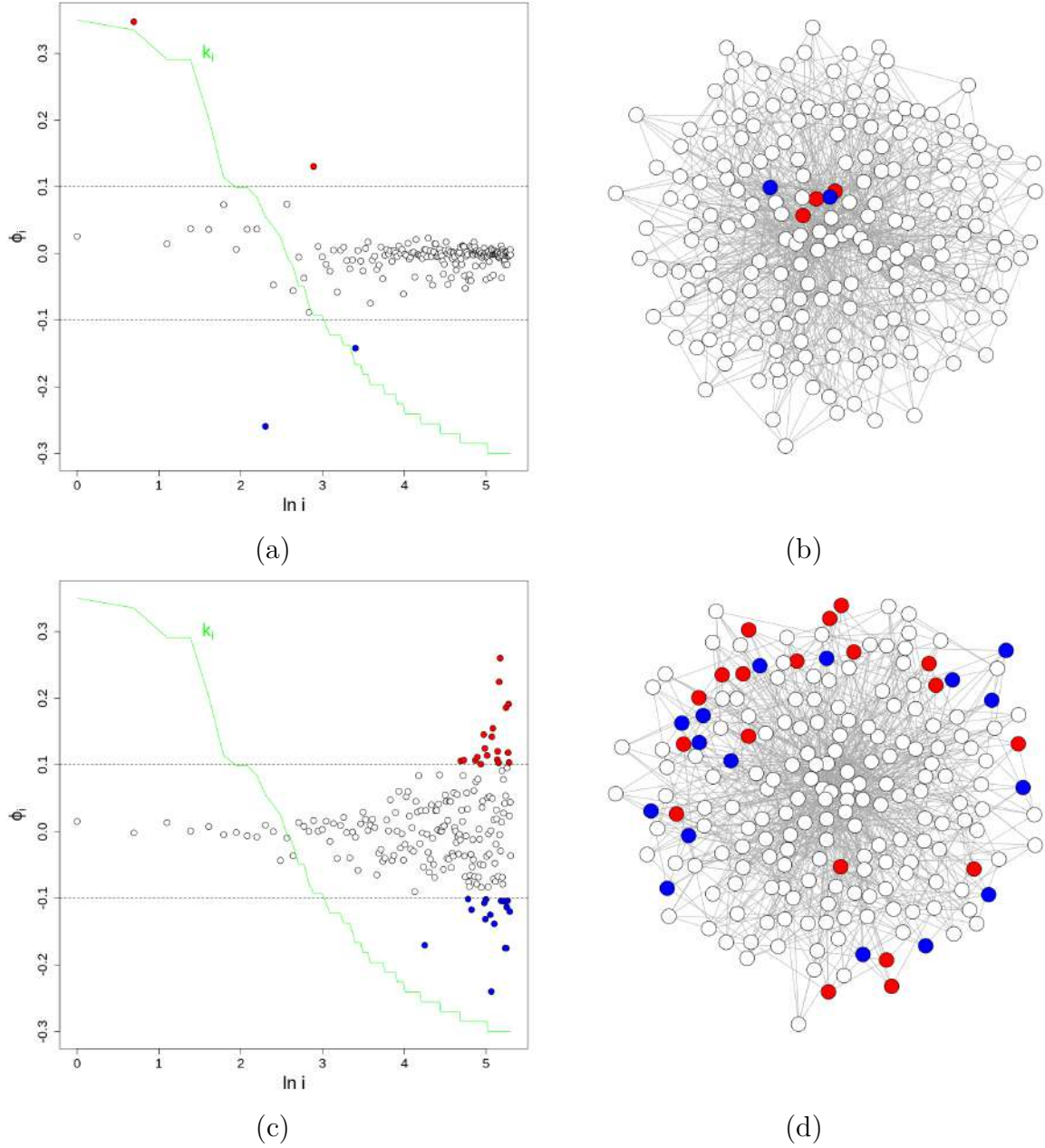


Figure 1.2: Nodes differentiation visualized with critical eigenvectors $\phi^{(\alpha_c)}$ for $\alpha_c = 190$ (a) and $\alpha_c = 15$ (c). On the right the differentiated eigenvectors are visualized on the network for the same value of $\alpha_c = 190$ (b) and $\alpha_c = 15$ (d), corresponding respectively to $\epsilon = 0.06$ and $\epsilon = 0.425$. The nodes are colored in red if $\phi_i^{(\alpha_c)} \geq 0.1$ and in blue if $\phi_i^{(\alpha_c)} \leq -0.1$.

1.6.5 Stationary patterns and mean-field bifurcation plots

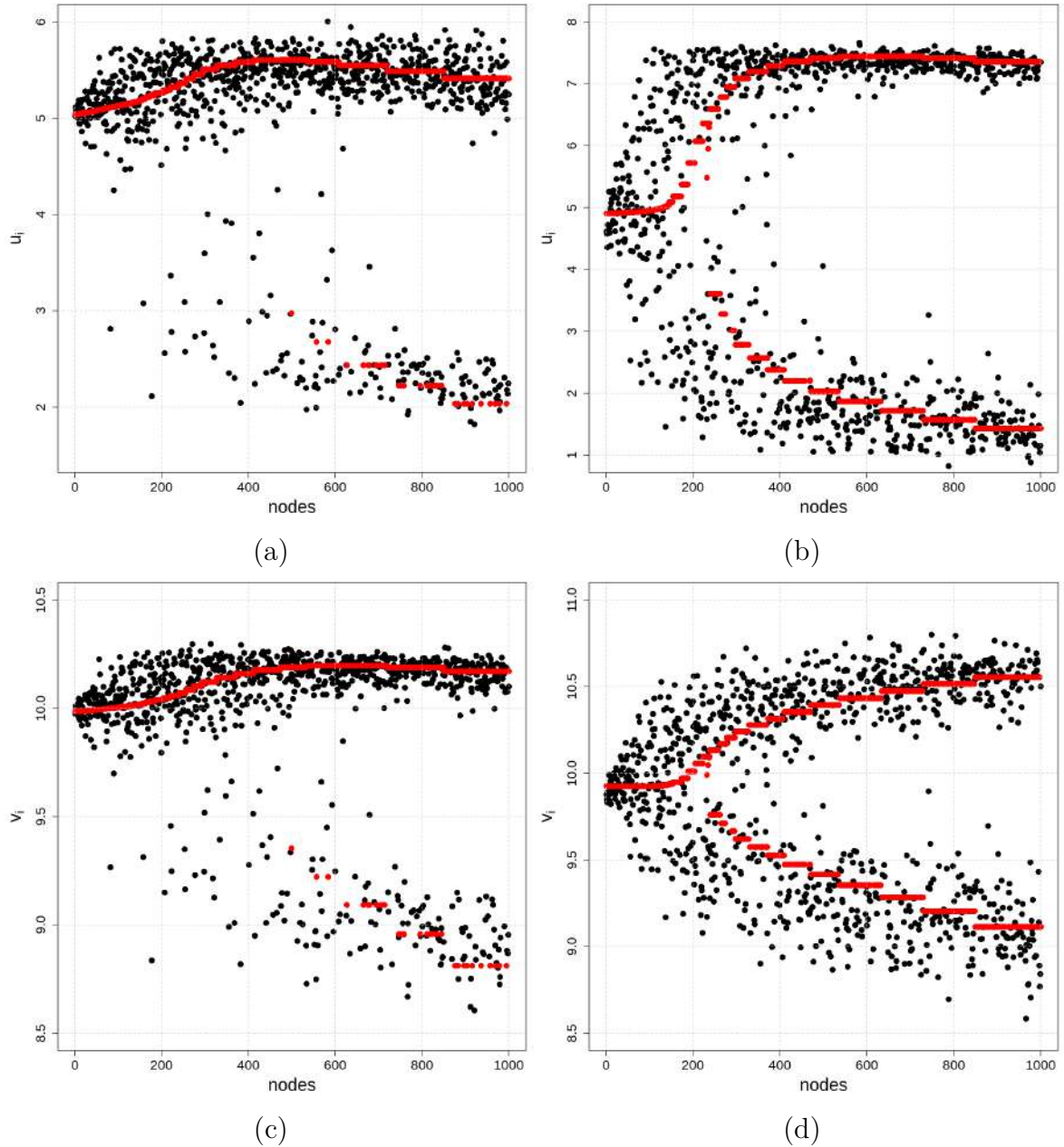


Figure 1.3: Stationary Turing patterns and mean-field bifurcation diagrams of the Mimura-Murray model on a scale-free network with $N = 1000$ and $\langle k \rangle \simeq 20$. Black dots are representing the stationary Turing patterns, while red ones are for the mean-field diagrams. Above (a,b) the activator densities, below (c,d) the inhibitor ones, on the left (a,c) plots for $\sigma = 15.6$, on the right (b,d) $\sigma = 30$ instead.

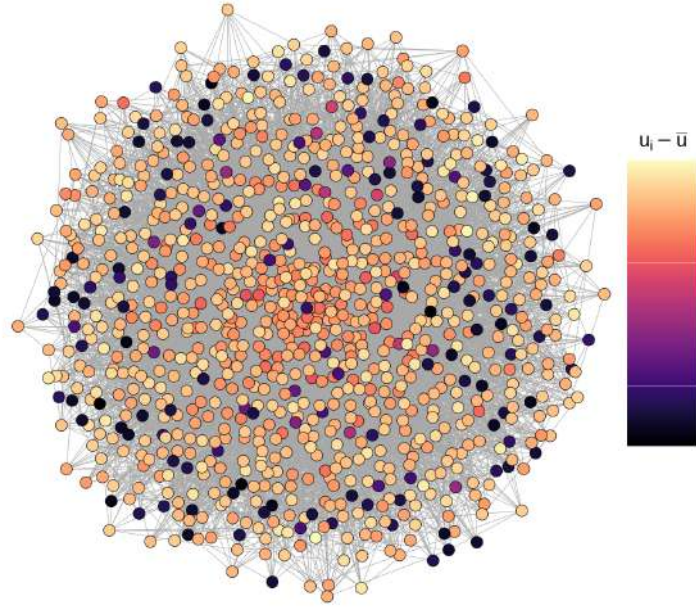


Figure 1.4: Plot of the used synthetic network, using as nodes color the difference between the activator density at stationarity and the uniform stable state \bar{u} . The plot is built in such a way that the hubs are in the middle and the nodes with lower degrees are located at the edges of the graph.

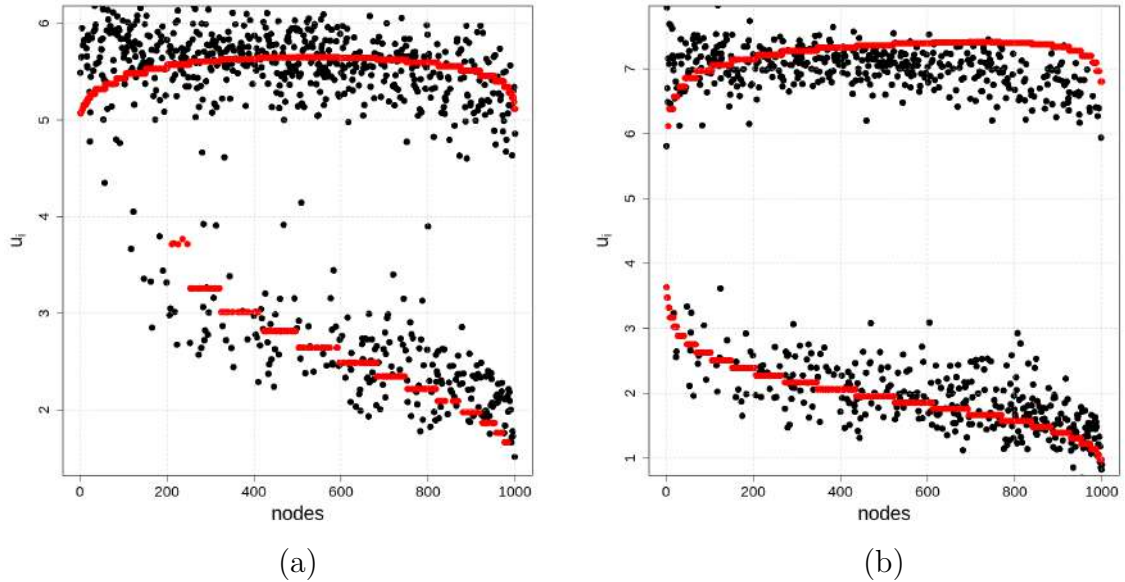


Figure 1.5: Stationary Turing patterns and mean-field bifurcation diagrams of the Mimura-Murray model on a Erdős–Rényi network with $N = 1000$ and $\langle k \rangle \simeq 20$. Black dots are representing the stationary Turing patterns of the activator, for $\sigma = 15.6$ (a) and $\sigma = 30$ (b).

2 | The Kuramoto model

Task leader(s): *Marco Chiloiro*

2.1 | Introduction

The need to understand synchronization, mainly in the context of biological neural networks, promoted the first studies of synchronization of coupled oscillators considering a network of interactions between them.

The Kuramoto model is a mathematical model used in studying synchronization by describing the behavior of a large set of coupled limit cycle oscillators [2]. The population of oscillators exhibits the dynamic analog to an equilibrium phase transition. When the natural frequencies of the oscillators are too diverse compared to the strength of the coupling, they are unable to synchronize and the system behaves incoherently. On the other hand, if the coupling is strong enough, all oscillators freeze into synchrony. The transition from one regime to the other takes place at a certain threshold. This constitutes the *onset of synchronization*.

In this paper, we numerically study the synchronization of coupled phase oscillators following the Kuramoto model (KM) on different underlying topologies, specifically on Erdős–Rényi (ER), Watts–Strogatz (WS) and Barabasi–Albert (BA) networks. The latter model is of particular interest because it aims to reproduce real networks with scale-free (SF) topology, since the degree distribution follows the power law $P(k) \sim k^{-3}$. Moreover, it has been shown [3], using that network, that high densely interconnected sets of oscillators synchronize more easily than those with sparse connections. Finally, we analyze synchronization dynamics in complex networks with hierarchical organization of communities [1] and how this process unravels its different topological scales.

2.2 | Theoretical background

The Kuramoto model on complex topologies consists of a population of N coupled interacting oscillators where the phase of the i -th unit, named $\theta_i(t)$, evolves in time according to the following dynamics

$$\dot{\theta}_i = \omega_i + \lambda \sum_{j=1}^N A_{ij} \sin(\theta_j - \theta_i) \quad (i = 1, \dots, N), \quad (2.1)$$

where ω_i stands for its natural frequency, K_{ij} describes the coupling between units and A_{ij} are the adjacency matrix elements representing the connectivity of the considered topology. The frequencies ω_i are distributed according to some function g , that is usually assumed to be unimodal and symmetric about its mean frequency ω_0 .

The original KM assumed an all-to-all purely sinusoidal coupling, i.e. $A_{ij} = 1 - \delta_{ij}$ and $\lambda = K/N$. In this case, the onset of synchronization occurs at a critical value of the coupling strength $K_c = 2/\pi g(\omega_0)$. It is possible to demonstrate, by using the mean field approximation, that [2]

$$\lambda_c = K_c \frac{\langle k \rangle}{\langle k^2 \rangle}, \quad (2.2)$$

where λ_c is the critical value of the coupling strength for a generic complex network with large enough average degree $\langle k \rangle$.

The second-order phase transition is characterized by the following macroscopic order parameter

$$r(t) = \left| \frac{1}{N} \sum_{j=1}^N e^{i\theta_j(t)} \right|, \quad (2.3)$$

which represents the phase coherence of the population. The values $r \simeq 1$ and $r \simeq 0$ (\simeq because fluctuations of size $O(N^{-1/2})$) describe the limits in which all oscillators are either phase locked or move incoherently, respectively.

If the oscillators are identical, i.e. $\omega_i = \omega$, $\forall i = 1, \dots, N$, the only attractor of the dynamics is the fully synchronized state where $\theta_i = \theta$, $\forall i = 1, \dots, N$. For a complex network with a hierarchical connectivity pattern, the dynamical route towards the global attractor reveals, at different time scales, different topological structures, those which represent communities. The different time scales at which different topological scales appear are related to the spectrum of the combinatorial Laplacian matrix \mathbf{L} . To study this phenomenon, we consider a local order parameter measuring the average (over initial random phases) of the correlation between pairs of oscillators

$$\rho_{ij}(t) = \langle \cos(\theta_j(t) - \theta_i(t)) \rangle. \quad (2.4)$$

2.3 | Emergence of spontaneous synchronization

In order to inspect the dynamics of the N oscillators on top of complex topologies, we perform numerical simulations of the model in different networks ($N = 100$ nodes per network). Starting from $\lambda = 0$, we increase at small intervals its value. Then, we integrate the equations (2.1) over a sufficiently large period of time ($M = 500$) to ensure that the system is in a stationary state and the order parameter r is computed. The procedure is repeated gradually increasing λ until the system evolves to a state of collective phase synchronization. The initial phases $\{\theta_i\}_{i=1, \dots, N}$ and the natural frequencies $\{\omega_i\}_{i=1, \dots, N}$ are randomly drawn from a uniform distribution in the interval $(-\pi, \pi)$ and $(-1/2, 1/2)$ respectively. The global dynamics of the system is qualitatively the same for all the tested networks, as shown in Fig. 2.1. As coupling strength increases, interactions remain weak initially, unable to counteract individual dynamics. Beyond a critical value λ_c , some elements lock in phase, initiating synchronization. With further increase, oscillators split: a partially synchronized group increases the order parameter r , while others stay different. As coupling strengthens, more nodes entrain, reaching complete synchronization ($r \simeq 1$). Besides, more is the connectivity of the used network, i.e. more is its average degree $\langle k \rangle$, and less is the critical point, meaning that it is necessary less coupling strength to reach the synchronization of the system. Moreover, (2.2) suggests that the critical coupling strongly depends on the

topology of the underlying graph: fixed $\langle k \rangle$, more the studied network is heterogeneous and less is the critical coupling.

2.4 | Stability of the synchronous state

Now we look at the stability of the synchronous state for a KM implemented on a BA network with $N = 300$ nodes and average degree $\langle k \rangle = 2m = 6$, where $m = 3$ is the number of edges that the nodes added at each time step have during the formation of the network. In order to do that, we compute the average time $\langle \tau \rangle$ it takes for a node of degree k to be again in a synchronized cluster after being perturbed and put out of synchronization. We consider a system already in a synchronized state, and we subtract from the phase of a randomly selected node i of degree k_i an angle equal to $-\pi$. After that, we measure the time it takes for i to recover from the perturbation. An example of this process is shown in Fig. 2.2. We can see that as λ is high enough (in this case $\lambda = 0.6$), the oscillator i ends up in the synchronous state with the same phase it had before being perturbed. By performing a least-square fit of the type $\langle \tau \rangle = A + Bk^{-1}$, we find that there is a clear power law dependency $\langle \tau \rangle \sim k^{-\gamma}$, with $\gamma \simeq 1$, as shown in Fig. 2.3. Therefore, the more connected a node is, the more stable it is. Besides, it is easy for an element with high degree k to get locked in phase with its neighbors than for a node weakly connected. This fact may suggest an explanation for the last discussed observation in the previous section. Since the BA model present more heterogeneity than the other two studied networks, it has a greater number of nodes with high connectivity and hence the lowest value of the critical coupling.

2.5 | Topological scales emergence by synchronization

Let us consider the following class of complex network: $N = 256$ nodes are grouped in 16 compartments that represents the first community organizational level, and 4 compartments containing each one 4 different compartments of the first level, that define the second organizational level of the network. Naming the average degree of nodes at first level k_{in1} , at second level k_{in2} and with any community of the rest of the network k_{out} , the network keeps a total average degree $k_{in1} + k_{in2} + k_{out} = 18$. From now on, these networks are indicated as k_{in1} - k_{in2} . Now we apply the KM (2.1) on the networks 13-4 and 15-2 at a given time t with all natural frequencies set to 0. We can see from Fig. 2.4 that the network 13-4 is very close to a state in which the 4 large groups are almost synchronized whereas the network 15-2 still presents some of the smaller groups of synchronized oscillators, and the larger group starting to synchronize, coherently with their topological structure. This fact highlights that different topological scales emerge by synchronization at different time scales. Moreover, these time scales depend on the spectrum of the combinatorial Laplacian matrix \mathbf{L} , as the inverse of its eigenvalues is a good quantitative measure of the stability of the structure (see 2.6.1 for more details).

2.6 | Appendix

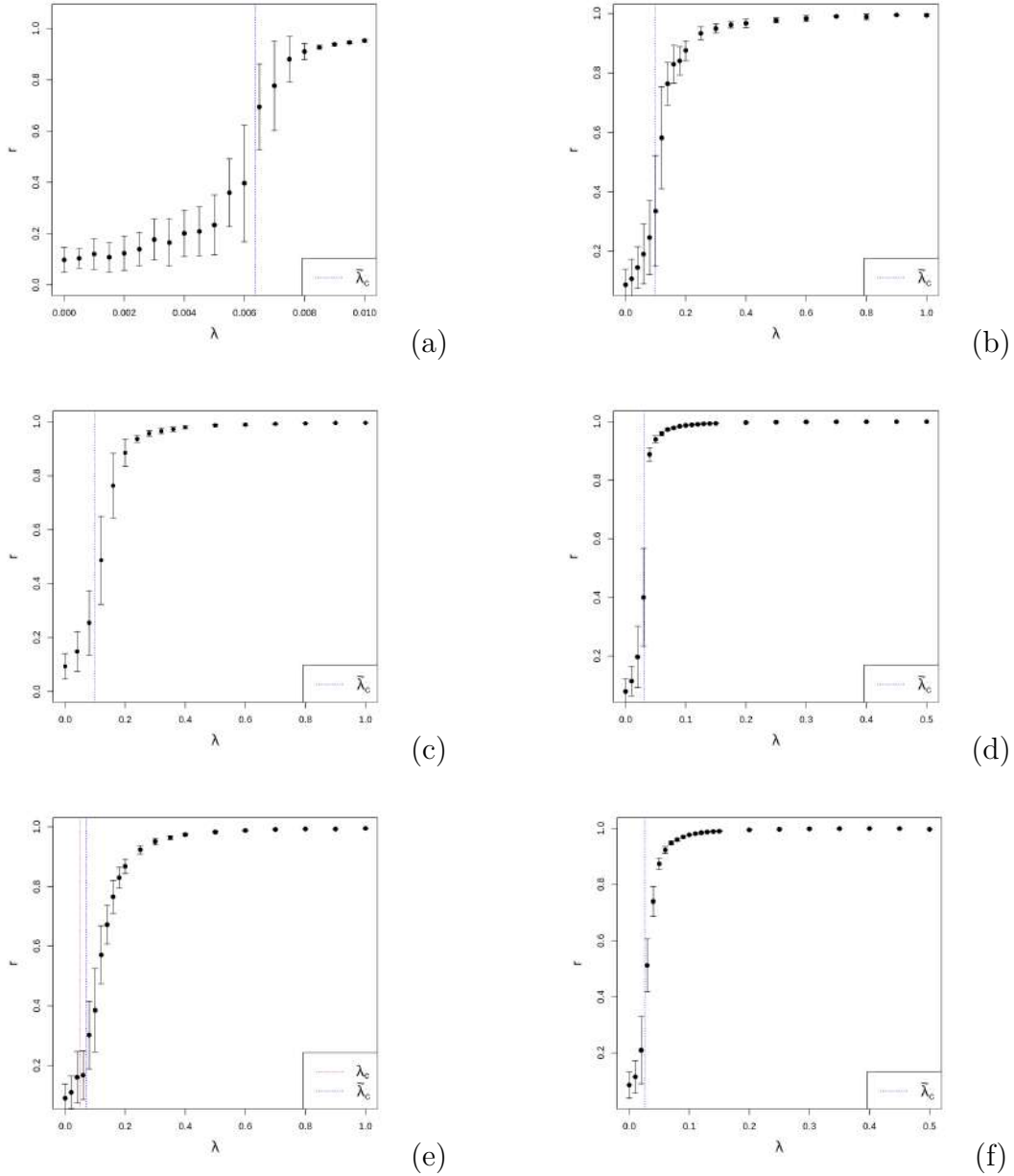


Figure 2.1: Coherence r as a function of λ for several artificial networks. Each value of r is the result of 5 network realization and 5 different initial conditions for each network realization. The critical coupling strength $\tilde{\lambda}_c$ is estimated by using the equation (2.2). (a) All-to-all network, i.e. an ER network with wiring probability $p = 1$. This model corresponds to the original KM, in this case $\tilde{\lambda}_c = K_c/N = 0.006$. (b) ER network with $p = 0.06$, corresponding to an average degree of $\langle k \rangle = p(N - 1) \simeq 6$. (c), (d) WS networks with rewiring probability $p = 0.2$ and average degree $\langle k \rangle = 6$ and $\langle k \rangle = 20$ respectively. (e), (f) BA networks with $\langle k \rangle = 2m = 6$ and $\langle k \rangle = 2m = 20$ respectively. In (e) the red dotted line represents the computationally computed value of coupling strength $\lambda_c = 0.05$ [3].

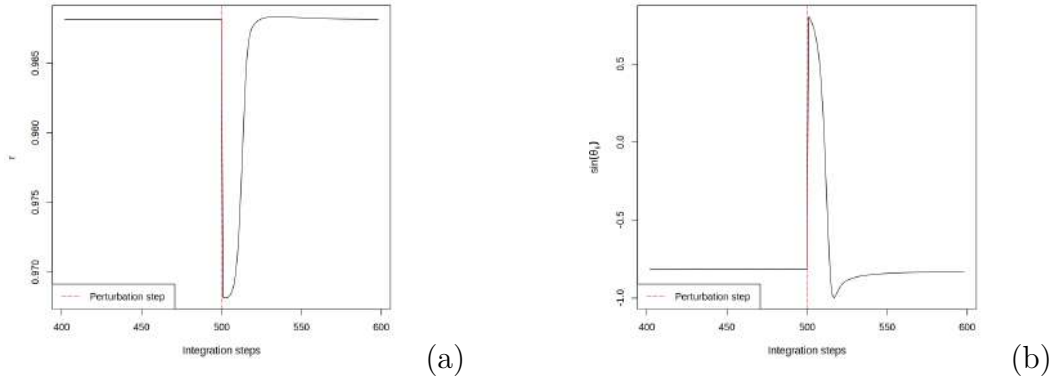


Figure 2.2: Perturbation on a randomly selected oscillator i of degree k_i and phase θ_i while it is in a synchronized state. λ is set to 0.6 (a) Plot of $\sin(\theta_i)$ versus the number of integration steps. (b) Plot of the order parameter r versus the number of integration steps.

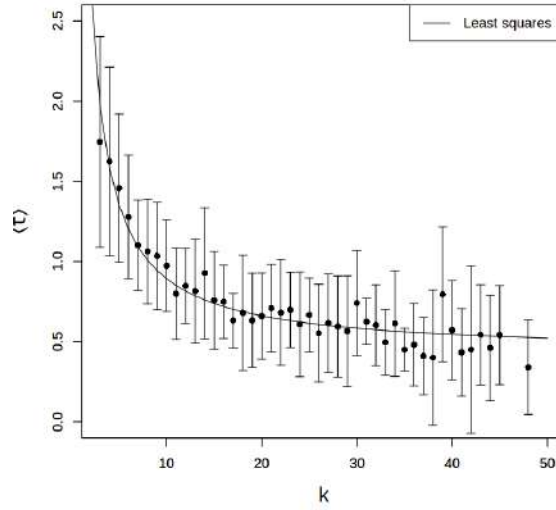


Figure 2.3: Plot of the dimensionless average time $\langle \tau \rangle$ (mean number of steps times the step size) it takes for a node of connectivity k to be back in the synchronous state after being perturbed, and the least-square fit of the type $\langle \tau \rangle \propto k^{-1}$. The results were average over 10 network realizations and at most 20 perturbations for each k .

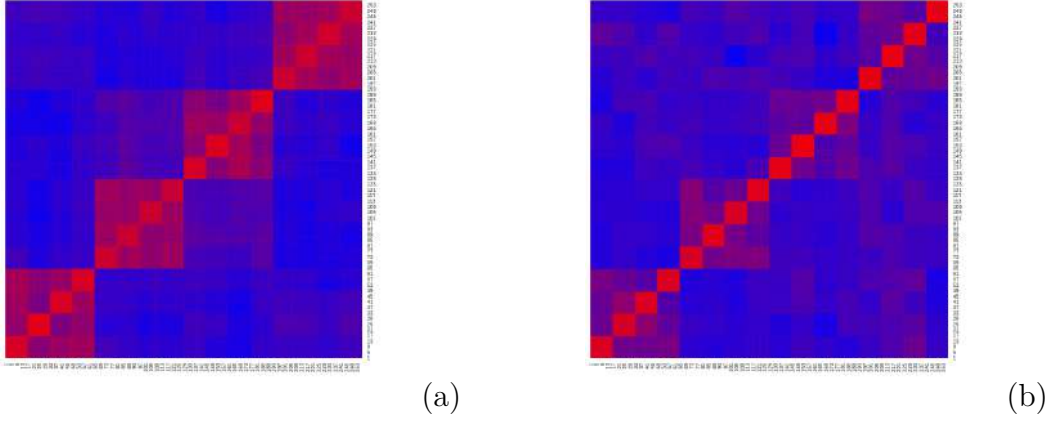


Figure 2.4: Heatmaps representing the correlation matrix $\rho_{ij}(t)$ defined by equation (2.4) for (a) 13-4 and (b) 15-2 networks computed at the same time t . The colors are a gradation between blue (-1) and red (1).

2.6.1 Linearized dynamics of the Kuramoto model

Let us consider the KM (2.1). If all the natural frequencies are set to 0, there is only one attractor of the dynamics. The dynamics close to the attractor of synchronization can be written as

$$\dot{\theta}_i(t) \simeq \lambda \sum_{j=1}^N A_{ij}(\theta_j(t) - \theta_i(t)). \quad (2.5)$$

We can express the last equation in terms of the combinatorial Laplacian matrix \mathbf{L} as follows

$$\dot{\theta}_i(t) \simeq \sum_{j=1}^N A_{ij}\theta_j(t) - k_i\theta_i(t) = \sum_{j=1}^N (A_{ij} - D_{ij})\theta_j(t) = -\sum_{j=1}^N L_{ij}\theta_j(t) \quad (2.6)$$

where $\lambda = 1$ for simplicity and \mathbf{D} is the degree matrix whose elements equals $D_{ij} = \delta_{ij}k_i$ for undirected networks. Then, the linearized dynamics of the Kuramoto model in compact form is

$$\dot{\boldsymbol{\theta}}(t) \simeq -\mathbf{L}\boldsymbol{\theta}(t). \quad (2.7)$$

The combinatorial Laplacian matrix can be diagonalized as $\mathbf{L} = \mathbf{Q}\mathbf{\Lambda}\mathbf{Q}^T$. Then we can write the equation (2.7) as

$$\dot{\boldsymbol{\phi}}(t) \simeq -\mathbf{\Lambda}\boldsymbol{\phi}(t), \quad (2.8)$$

where $\boldsymbol{\phi}(t) = \mathbf{Q}^T\boldsymbol{\theta}(t)$ is the vector collecting the normal modes $\phi_i(t)$ at time t . The last equation is no more a coupled system of differential equations, since $\mathbf{\Lambda}$ is diagonal. Then, the N solutions of (2.8) are

$$\phi_i(t) = e^{-\lambda_i t} \phi_i(0), \quad (2.9)$$

where λ_i are the eigenvalues of \mathbf{L} . We can see from (2.9) that the time scales for which each normal mode decays are the inverse of the eigenvalues $1/\lambda_i$, then, modes associated to the largest eigenvalues decays faster than the others. We know that the higher the degree of a node is, the faster its synchronization process is. Hence, the presence of large eigenvalues stands for the existence of highly connected nodes (hubs)

in the network.

If we rank the eigenvalues λ_i in descending order, the associated modes (2.9) tends to 0 in a hierarchical way as time increases. From Fig. 2.5 we can see that the time scales $1/\lambda_i$ corresponding to the ranks $i = 17$ and $i = 16$ are quite different, as well as for $i = 5$, $i = 4$. This means that the 16 modes associated to the lowest eigenvalues are noticeably more stable than the others, and again the 4 modes associated to the lowest eigenvalues are even more stable. This behavior highlights the hierarchical structure of the network: the nodes within the 16 organizational first-level communities synchronize first. The reached state of the system remains stable for a time of the order of $1/\lambda_{17} - 1/\lambda_{16}$, after which the nodes within the 4 second-level communities begin to synchronize. Again, when the second-level communities are synchronized, after a time of the order $1/\lambda_5 - 1/\lambda_4$ the nodes begin to synchronize toward the fully synchronized state of the system. Notice that for the 13-4 network, the time scale difference $1/\lambda_{17} - 1/\lambda_{16}$ is shorter than the $1/\lambda_5 - 1/\lambda_4$ one, and the contrary for the 15-2 case, indicating that the 16 clusters community is less well-defined in the former case.

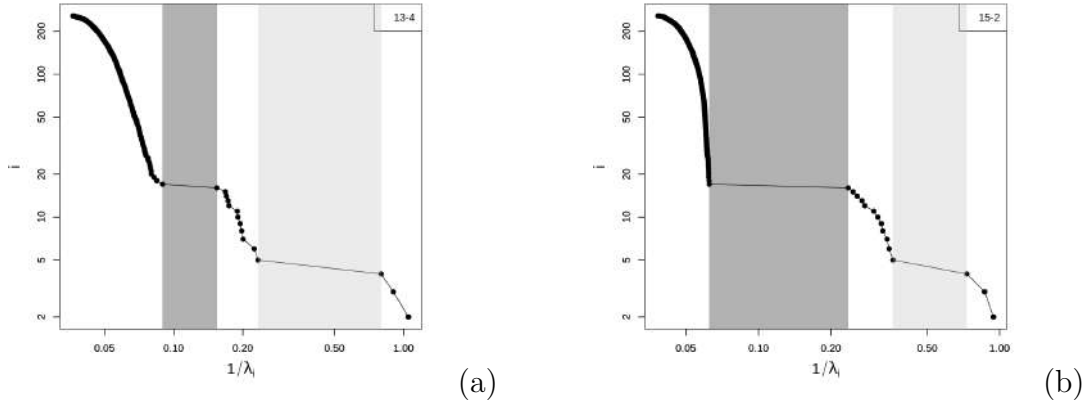


Figure 2.5: Rank index i versus the inverse of the corresponding eigenvalues λ_i of the combinatorial Laplacian matrix \mathbf{L} for (a) 13-4 and (b) 15-2 networks. The shadow regions indicate the stability plateaus in the eigenvalue spectrum corresponding to indices 16 (dark) and 4 (light) communities.

3 | Swarmalators dynamic

Task leader(s): *Campagnola Stefano, Bergamin Eleonora*

3.1 | Introduction

Swarmalators represent a system of self-organizing entities that exhibit synchronized behavior, similar to that of a swarm or a flock. The term is a combination of "swarm" and "oscillator", emphasizing the dual nature of the system's dynamic. These entities interact with each other and adjust their oscillatory patterns based on the local information they receive from neighboring swarmalators.

Swarmalator systems are commonly studied in the field of complex systems and swarm intelligence [5], [6]. They provide a simplified model for understanding and analyzing the emergence of collective behavior observed in various natural systems, such as bird flocks, fish schools, or insect swarms.

In our work, we analyze some properties of the system like steady state configurations under different interactions. We start from the model firstly developed in [5], which displays five different stationary distributions. We subsequently investigate the impact of external forcing on the phenomenon of phase synchronization, which has been previously addressed in [6], as well as time-varying interactions that resemble a temporal network connecting the entities. Lastly, we study a noisy variant of the initial model that incorporates an additional degree of freedom for orientation, leading to alignment phenomena. The latter is inspired by Vicsek's work on collective motion.

3.2 | Theoretical background

The main model discussed in this work can be summarized by the following set of differential equations:

$$\dot{\mathbf{x}}_i = \frac{1}{N} \sum_{\substack{j=1 \\ j \neq i}}^N \left[\frac{\mathbf{x}_j - \mathbf{x}_i}{|\mathbf{x}_j - \mathbf{x}_i|} (1 + J \cos(\theta_j - \theta_i)) - \frac{\mathbf{x}_j - \mathbf{x}_i}{|\mathbf{x}_j - \mathbf{x}_i|^2} \right] + v_0 \hat{\mathbf{n}} + \xi_i^{\mathbf{x}}(t) \quad (3.1)$$

$$\dot{\theta}_i = \omega_i + \sum_{\substack{j=1 \\ j \neq i}}^N \left[\frac{\sin(\theta_j - \theta_i)}{|\mathbf{x}_j - \mathbf{x}_i|} \left(\frac{K_{ij}^{att}}{N_i(r)} + \frac{K_{ij}^{rep}}{N - 1 - N_i(r)} \right) \right] + F \frac{\cos(\Omega t - \theta_i)}{|\mathbf{x}_0 - \mathbf{x}_i|} + \eta_i(t) \quad (3.2)$$

The first equation states that swarmalators have the ability to either attract or repel each other in space, and this behavior depends on both the distance and phase difference between them. The second equation explains how the internal phase variable

θ of each swarmalator can change. This change is determined by the aforementioned distance and phase difference, as well as external periodic perturbations.

Essentially, the main parameters involved in the dynamic are five. J is the strength of spatial attraction or repulsion due to phase similarity. K_{ij}^{att} and K_{ij}^{rep} are two matrices that express the magnitude of phase attraction or repulsion between two given swarmalators. F is then the external driving strength, while r is the phase interaction range. Spatial dynamics can also be driven by an intrinsic velocity v_0 of direction $\hat{\mathbf{n}} = (\cos \beta, \sin \beta)$, where β for now is the same for all the entities. Phase dynamic can instead be modulated by intrinsic angular frequencies ω_i . The two white noises $\xi_i^x(t)$ and $\eta_i(t)$ are considered only in the stochastic version of the model.

3.3 | Basic model

Firstly, we consider the deterministic model with only attractive coupling constants, setting $K_{ij}^{att} = K$ and $K_{ij}^{rep} = 0 \forall i, j$ in equation 3.2, and no perturbations from the outside ($F = 0$). We also leave the range of phase interaction r to be free to go to infinity, resulting in the number of neighbors $N_i(r) = N - 1$. We do not consider the term ω_i too for now, and v_0 is zero.

This swarmalators' system's behavior depends only on the two coupling strengths J and K . The system settles into five stationary states, depending on the values chosen for the couple (J, K) . Three of them can be considered static, while the other two display a visible flux of particles.

States description Since space dynamic is always attracting independently of J (given that $|J| \leq 1$), swarmalators will always aggregate within a delimited region of space (Fig. 3.1). If $K > 0$ the only possible behavior is synchronization (*static sync*), while for $K \leq 0$ different phenomena arise. If attraction strength J is negative or weak in the positive sign, *static async* configuration occurs and particles display a heterogeneous phase distribution. Increasing this parameter leads to the appearance of global rotating circles in the *active phase wave* state, until motion is restricted locally among the originated clusters of swarmalators (*splintered phase wave*). In the special case $K = 0$ and $J > 0$ only the spatial dynamic is involved, and the system reaches a stationary configuration that resembles a *static phase wave*.

Angular phase distribution Switching now to polar coordinates (r, φ) , it's interesting to distinguish the five aforementioned states on the basis of φ - θ correlation (Fig. 3.2). It can be observed that, in the *phase wave* states, angular alignment gradually arises. Instead, if we let evolve the *active phase wave* state, we would see two opposite currents flowing inside the stripes.

3.4 | Forced model

Interesting phenomena arise when we introduce an external driver to the basic model. The stimulus is placed at the center of the frame of reference, $\mathbf{x}_0 = (0, 0)$, with an angular frequency of $\Omega = 3\pi/2$. By progressively increasing F , synchronization with the external pulse spreads and affects the whole system in the end. In Fig. 3.3 this can

be seen clearly for all the five "stationary"¹ states. The most interesting behavior is the one of the *static phase wave* and *splintered phase wave* when $F = 1$. Swarmalators divide into two poles of opposite phase.

3.5 | Time varying interaction model

Proximity (in terms of range of interactions) can play a significant role in the description of the emergence of clustering phenomena. In this section, we exploit the idea of random geometric graph in network science to build a model in which neighbors interact differently with respect to the rest of the world. We set $K_{ij}^{att} = K_a$ and $K_{ij}^{rep} = 0$ if particles i and j are closer than r , otherwise $K_{ij}^{att} = 0$ and $K_{ij}^{rep} = K_r$. The terms associated to the external forcing and noise in equations 3.1 and 3.2 are turned off. For a given combination of the parameters J , r , K_a and K_r we can see from Fig. 3.4 that swarmalators subdivide in two distinct components (π state), while in other cases a unique giant component emerges, hosting smaller fading subgroups of entities with similar phase (*mixed phase wave*).

3.6 | Vicsek model

In many systems, individuals that swarm and sync tend also to align their own motion with the one of the neighbors. This type of scenario has been quite studied by Vicsek in [7]. From the mathematical point of view, we endow swarmalators of an orientation β_i that is no more global and follows the equation below:

$$\dot{\beta}_i = -\beta_i + \frac{1}{|\Lambda_i(\delta)|} \sum_{j \in \Lambda_i(\delta)} \beta_j + \zeta_i(t) \quad (3.3)$$

Direction of a given entity i will be conditioned only by neighbors (indicated with $\Lambda_i(\delta)$) within a distance δ from it. Considering all the three dynamic equations, parameters are set as follows. Starting from the *Basic Model*, we add some intrinsic angular frequencies ω_i that are drawn from a Lorentzian distribution of $HWHM = \sigma$ and we also allow some position, phase and alignment disorder ($\xi_i^x(t)$, $\eta_i(t)$, $\zeta_i(t)$) of strengths D_θ , D_β . Intrinsic velocity v_0 is now different from zero and its direction is ruled by $\hat{\mathbf{n}} = (\cos \beta_i, \sin \beta_i)$. This is the equation term describing the interaction between position and orientation, used to investigate the alignment's effects on the system. In the equations, orientation and phase remain uncoupled.

In this model, simulations revealed that for the choice of parameters $K = (-0.1, -1)$ and $D_\beta = 0.01$ we are able to observe aligned states, with the swarmalators depicted as colored arrows in 3.5. In particular, the swarmalators aligned according to the parameter β while their distributions of space and phase remained similar to the basic model. However, unlike the original model, the center of mass shifted based on initial conditions, indicating mobility. A study of the movement of the center of mass is reported in the appendix. For higher alignment noise $D_\beta = 1.0$ unaligned states emerged as can be observed in 3.5.

¹they are not really stationary, because of the time dependent driver. It's more like a periodic pattern.

3.7 | Appendix

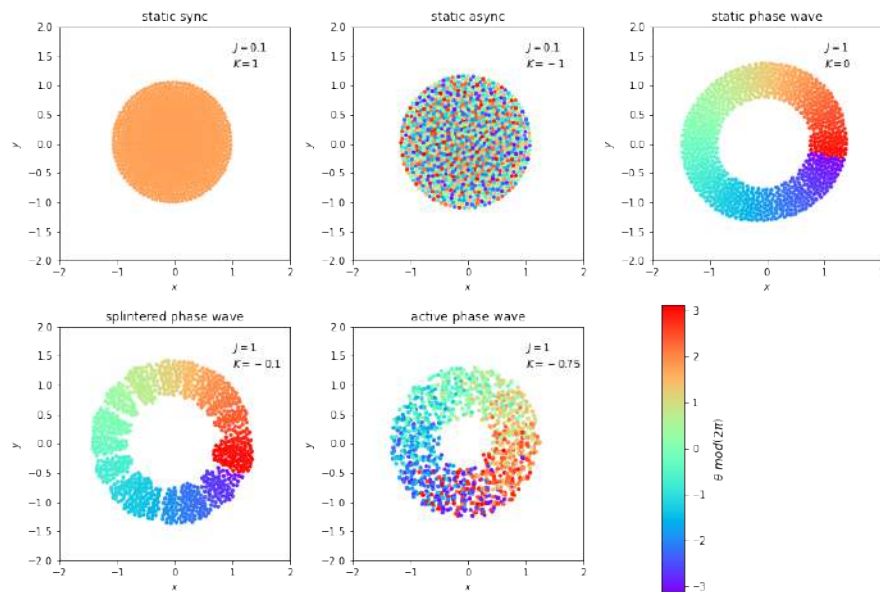


Figure 3.1: Basic model stationary states

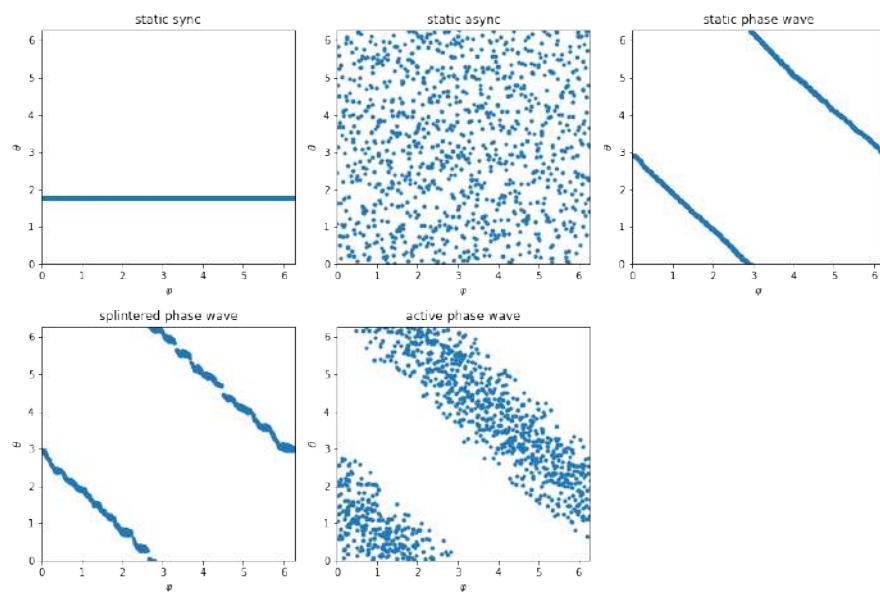


Figure 3.2: Basic model stationary states angular phase distribution

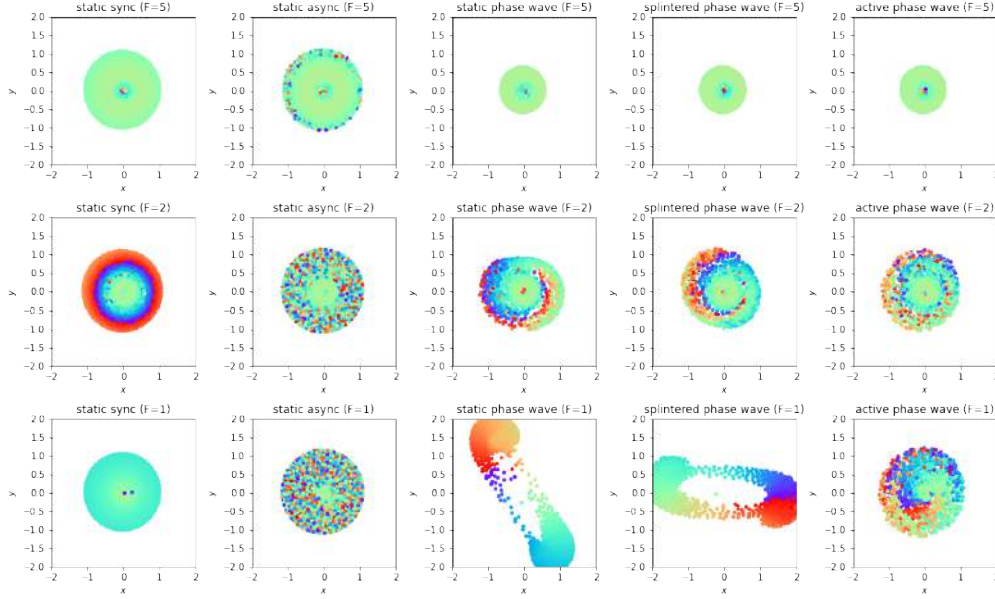


Figure 3.3: Forced model stationary states

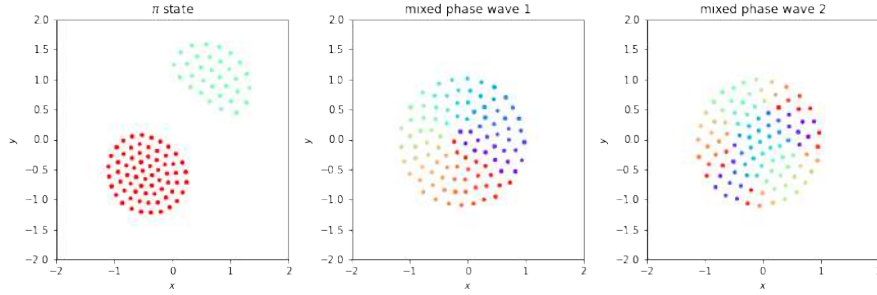


Figure 3.4: Time varying interaction model

3.7.1 Lattice model

In the cases analyzed so far, the interactions take place continuously. We now want to discretize the model and study spatial networks. In particular, we choose to consider a square lattice, of which we are going to vary the spacing.

To simulate the dynamics, we choose to constrain the positions of the swarmsalators to correspond to the nodes, we make the system evolve according to the dynamics equations already introduced, and finally we approximate the new position to that of the closest node.

We observe that considering a sufficiently small cell we obtain a dynamic analogous to the continuous case. By increasing the size of the cell, we see different behaviors depending on the system's state.

In the *active phase wave* regime, a square side of approximately $L > 0.001$ forces the swarmsalators to freeze in a *static async* configuration. In the *splintered phase wave* region, this threshold is greater and stands at $L \simeq 0.01$. This crystallization is given by the fact that the position changes are not large enough to allow the swarmsalators to change node. For the *static phase wave* no transition occurs, however with too large

value of L (namely $L > 0.006$) the algorithm fails, since multiple entities might want to occupy the same node. The same behavior also belongs to the *static sync* and *async*, where L cannot be too large.

3.7.2 Vicsek model

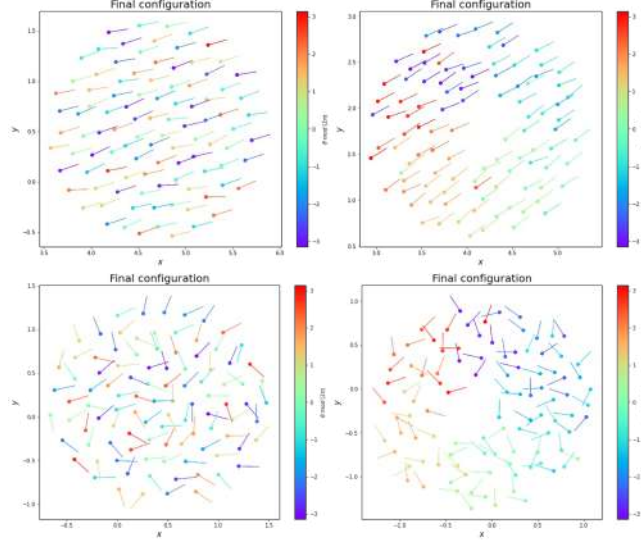


Figure 3.5: Vicsek model, integration step $dt = 0.1$, final time $T = 5000$, 100 swarmalators. Clockwise, the parameters are $(K, D_\beta) = (-0.1, 0.01)$, $(K, D_\beta) = (-1.0, 0.01)$, $(K, D_\beta) = (-0.1, 1.0)$, $(K, D_\beta) = (-1.0, 1.0)$.

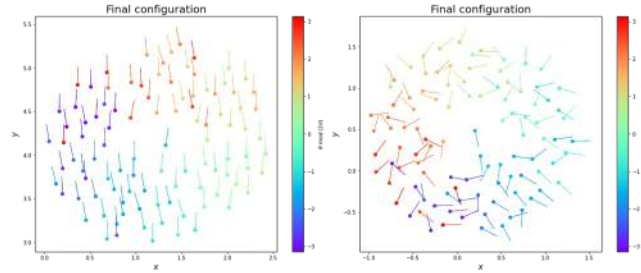


Figure 3.6: Vicsek model, integration step $dt = 0.01$, final time $T = 5000$, 100 swarmalators. Clockwise, the parameters are $(K, D_\beta) = (-1.0, 0.01)$, $(K, D_\beta) = (-1.0, 1.0)$.

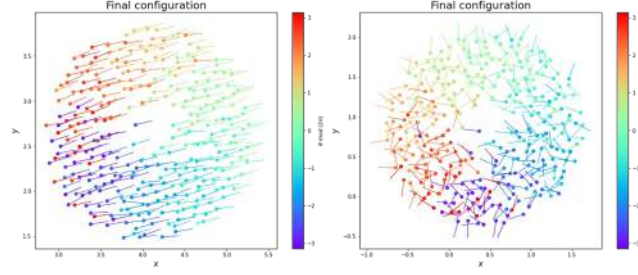


Figure 3.7: Vicsek model, integration step $dt = 0.1$, final time $T = 5000$, 300 swarmalators. Clockwise, the parameters are $(K, D_\beta) = (-1.0, 0.01)$, $(K, D_\beta) = (-1.0, 1.0)$.

Center of Mass dynamics

In this paragraph, we investigate the behavior of the center of mass in a system previously described in section 3.6. To study this behavior, we gradually increase the level of noise D_β from zero (resulting in deterministic dynamics) to one, with increments of 0.1, while keeping all other system parameters constant. We specifically focus on two cases: $K = -1.0$ and $K = -0.1$.

For each noise level, we calculate the distance between the initial and final positions of the center of mass. We perform this calculation for five different initial configurations of the swarmalators. Subsequently, we compute the mean and the error associated with these distance measurements.

To gain insights into how the data behaves, since we expect the distance to get to zero for a high enough noise level, we fit it to two different functions: an exponential fit and a power-law fit. During our analysis, we observe that the power-law fit provides a better description of the data and yields a smaller sum of the residuals.

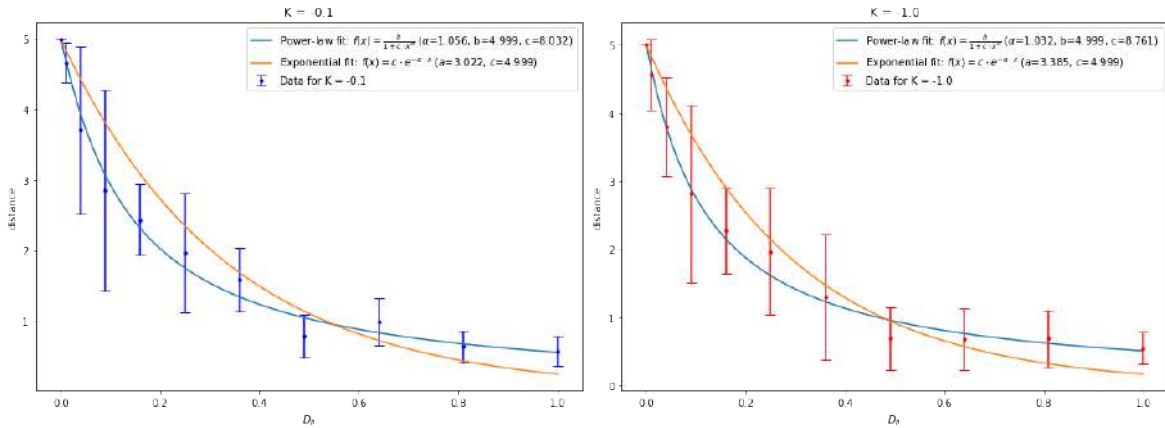


Figure 3.8: Measures of distance and both fits for $K = -0.1$ and $K = -1.0$

4 | Bibliography

- [1] Alex Arenas, Albert Díaz-Guilera, and Conrad J. Pérez-Vicente. Synchronization reveals topological scales in complex networks. *Physical Review Letters*, 96(11), mar 2006. doi: 10.1103/physrevlett.96.114102. URL <https://doi.org/10.1103/2Fphysrevlett.96.114102>.
- [2] Alex Arenas, Albert Díaz-Guilera, Jurgen Kurths, Yamir Moreno, and Changsong Zhou. Synchronization in complex networks. *Physics Reports*, 469(3):93–153, dec 2008. doi: 10.1016/j.physrep.2008.09.002. URL <https://doi.org/10.1016/2Fj.physrep.2008.09.002>.
- [3] Y Moreno and A. F Pacheco. Synchronization of kuramoto oscillators in scale-free networks. *Europhysics Letters (EPL)*, 68(4):603–609, nov 2004. doi: 10.1209/epl/i2004-10238-x. URL <https://doi.org/10.1209/2Fep1%2Fi2004-10238-x>.
- [4] Hiroya Nakao and Alexander S. Mikhailov. Turing patterns in network-organized activator–inhibitor systems. (6):544–550, apr 2010. doi: 10.1209/0295-5075/ac8445. URL <https://doi.org/10.1038/nphys1651>.
- [5] Kevin P. O’Keeffe, Hyunsuk Hong, and Steven H. Strogatz. Oscillators that sync and swarm. *Nature Communications*, 8(1), nov 2017. doi: 10.1038/s41467-017-01190-3. URL <https://doi.org/10.1038/2Fs41467-017-01190-3>.
- [6] Gourab Kumar Sar and Dibakar Ghosh. Dynamics of swarmalators: A pedagogical review. *Europhysics Letters*, 139(5):53001, aug 2022. doi: 10.1209/0295-5075/ac8445. URL <https://doi.org/10.1209/2F0295-5075/2Fac8445>.
- [7] Tamás Vicsek, András Czirók, Eshel Ben-Jacob, Inon Cohen, and Ofer Shochet. Novel type of phase transition in a system of self-driven particles. *Phys. Rev. Lett.*, 75:1226–1229, Aug 1995. doi: 10.1103/PhysRevLett.75.1226. URL <https://link.aps.org/doi/10.1103/PhysRevLett.75.1226>.